Zhang *et al. J Infrastruct Preserv Resil* (2023) 4:6
https://doi.org/10.1186/s43065-022-00070-5

Journal of Infrastructure Preservation and Resilience

RESEARCH

Open Access

Emerging steel frames with Fe-SMA U-shaped dampers for enhancing seismic resilience

Zhe-Xi Zhang, Jie Zhang, Cheng Fang*, Yuelin Zhang and Yuanmu Li

Abstract

Post-earthquake financial loss of structures induced by residual inter-story deformation (RID) has been recently noticed and various strategies have been proposed. A newly-emerged energy-dissipation material, namely, iron-based shape-memory-alloy (Fe-SMA), has gain favor in civil engineering community due to its extraordinary low-cycle fatigue resistance property. Besides, Fe-SMA is believed to help improve structure's post-earthquake residual inter-story deformation control capacity due to its moderate strain hardening behavior and pseudo-elasticity. This study explores the performance of emerging steel frame systems equipped with energy-dissipation devices fabricated with Fe-SMA. In particular, a brace with built-in Fe-SMA-based U-shaped strips (USSs) is employed serving as the energy-dissipation devices in the proposed system. In this paper, the basic mechanical properties of Fe-SMA are discussed firstly, followed by a description of the working principle of the USSs. The hysteresis behavior of two types of USSs, fabricated with Fe-SMA and conventional mild steel (Q235), were investigated experimentally. Based on the test results, numerical models for the prototype braces equipped with USSs are established using ABAQUS and OpenSEES, and the necessary key material parameters are calibrated. Subsequently, system-level analysis is performed on 5-story prototype steel buildings. Specially, two types of steel frames, i.e., frames with high-strength-steel columns and frames with conventional structural steel-based columns, are established. Concurrently, braces with Fe-SMA-based USSs as well as mild steel-based USSs are considered. The results demonstrated that the Fe-SMA-based energy-dissipation devices along with the steel frames with high-strength-steel columns can provide the most satisfied RID control effectiveness compared with the other yielding structural systems investigated in this paper.

Keywords Iron-based shape memory alloy (Fe-SMA), Fe–Mn-Si-Cr-Ni alloy, U-shaped damper, Seismic performance, Residual inter-story deformation (RID)

Introduction

Buildings designed by conventional seismic design philosophy (so-called conventional yielding structural systems) have been proven to be safe during earthquakes. However, post-earthquake recoverability cannot be guaranteed. For example, hundreds of buildings that did not collapse were demolished after the 2011 Christchurch earthquake [1] due to unacceptable damage and excessive residual inter-story deformation (RID). The 1995 Kobe earthquake [2] led to the removal of more than 90 non-collapsed reinforced concrete (RC) bridge piers whose residual drifts exceeded 1%. Since post-earthquake loss induced by large RID (larger than 0.5%) is often difficult to deal with [3], it is critical to consider residual deformation as a supplementary seismic performance index in structural design.

Driven by this demand, the concept of self-centering structural system providing a controllable RID for

*Correspondence:
Cheng Fang
chengfang@tongji.edu.cn
Department of Structural Engineering, College of Civil Engineering, Tongji University, Shanghai 200092, China

post-earthquake structures has been proposed. Existing self-centering strategies are mainly realized by utilizing self-centering prestressing assemblies, super-elasticity materials, or self-centering tendency induced by gravity [4–9].'Flag-shaped' hysteresis behavior with negligible residual deformation (near zero) is achieved because of these self-centering strategies. Ricles et al. [6] developed post-tensioned moment-resisting connections with seat angles serving as energy-dissipation source. Christopoulos et al. [10] proposed a new self-centering energy dissipative bracing system with tensioning elements and friction pads involved. Tsai et al. [11] proposed a post-tensioned steel beam-to-column connection constructed with bolted web friction devices. Chou et al. [12] proposed and investigated a dual-core self-centering sandwiched buckling restrained brace with enhanced deformability. On the other hand, self-centering strategy that utilizes super-elasticity materials, specifically, NiTinol-based shape memory alloy (NiTi-SMA), has been investigated in recent 20 years. Fang and colleagues systematically explored the effectiveness of NiTi-SMA-based elements such as cables [13, 14], washers [15, 16], ring springs [17, 18] and bolts [19], for promoting the self-centering capability of steel frames. Qiu and Zhu [20] experimentally investigated the seismic performance of steel frames equipped with NiTi-SMA braces. Outstanding RID control capacity is confirmed for such frames even if the peak inter-story drift (PID) ratio exceeded 2%. Additional energy dissipative materials/elements have been considered in these strategies. For example, Chen et al. [21] proposed a novel variable friction damper that cooperate the NiTi-SMA cables and friction devices. Ping et al. [22], and Zhang et al. [23] proposed NiTi-SMA viscoelastic hybrid self-centering braces to reach a moderate damping ratio. System-level analyses demonstrate that the PID and RID can be effectively controlled by such solutions.

Satisfied RID control capacity is achieved by self-centering strategy, nevertheless, problems still exist when taking the following issues into consideration: 1) It has been revealed that the self-centering capability of the aforementioned self-centering structural system is achieved at the cost of decreased energy dissipation capacity, amplified peak deformation response, more pronounced high-mode effect and larger peak absolute floor acceleration, especially compared with those of conventional yielding systems [23]. 2) The ductility of self-centering structural system is limited by the ultimate elastic deformation range of self-centering components, beyond which range the structure may face the risk of sudden fracture under strong earthquakes [24]. 3) The poor low cycle fatigue (LCF) resistance of self-centering components should be seriously concerned, especially when self-centering structures are exposed to long-duration long-period earthquakes followed by aftershocks [25]. 4) The temperature dependence of NiTi-SMA and high cost may also jeopardize the practical application of NiTi-SMA [26, 27].

Based on these considerations, a new strategy that possess sufficient energy-dissipation capacity, ductility, and reasonable RID control capacity, needs to be proposed. Iron-based shape memory alloy (Fe-SMA) [25] may serve as a promising material to realize this idea. As shown in Fig. 1, the energy-dissipation capability of Fe-SMA is comparable to conventional mild steel and significantly higher than NiTi-SMA. Compared with conventional steels, Fe-SMA has a higher post-yield stiffness, which has been reported to be beneficial for reducing post-earthquake residual deformation of structures under seismic excitations [28]. Importantly, Fe-SMA possesses a certain degree of pseudo-elasticity behavior, a property which further contributes to reduction of residual deformation during dynamic shake down. On the other hand, Fe-SMA could have 5–10 times LCF life than that of conventional steels, a property which is attributed to its unique diffusionless solid state phase transformation [29]. In addition, Fe-SMA features good ductility (as typically shown in Fig. 2) [30], which provide sufficient room for components to deform under large amplitudes induced by severe earthquakes. These characteristics, along with its inherently low cost (probably comparable to that of stainless steel) [25], make Fe-SMA an ideal candidate for producing energy-dissipation (ED) devices in seismic resistance community. Laboratory-level experiments on Fe-SMA-based dampers, although limited, have been carried out. For example, Inoue et al. [31] investigated the

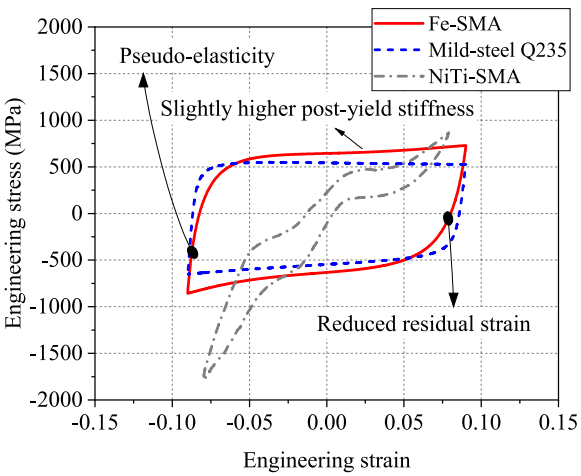

Fig. 1 Cyclic engineering stress–strain curves for Fe-SMA, mild-steel and NiTi-SMA [36]

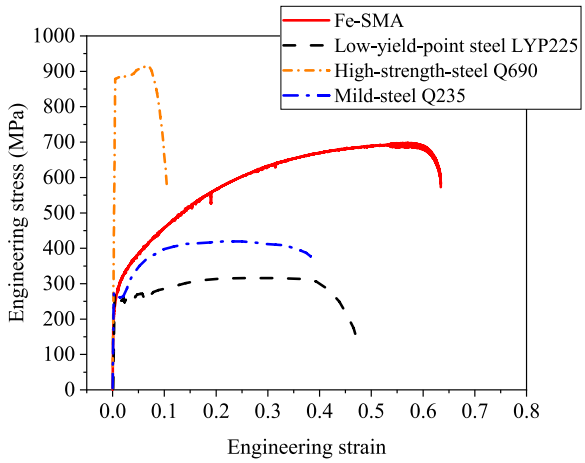

Fig. 2 Monotonic engineering stress–strain curves for Fe-SMA and some typical structural steels [25]

cyclic response of Fe-SMA-based buckling-restrained braces (BRBs). Ghowsi et al. [32] further studied the displacement ductility and energy-dissipation capacity of Fe-SMA-based BRBs. Fang et al. [30, 33, 34] carried out a series of proof-of-concept experiments on Fe-SMA-based shear damper and U-shaped damper and proved the outstanding LCF resistance of these novel metallic dampers. Wang and Zhu [35] conducted a systematic experimental investigation of the cyclic behavior of Fe-SMA bars with a buckling-restrained device. In practice, the first successful field application of Fe-SMA-based damper was the JP Tower, Nagoya, Japan, 2015 [31].

It can be seen that system-level analysis of Fe-SMA-based structures is still limited. To provide an in-depth insight into the seismic resistance performance of Fe-SMA-based ED devices (FED) in steel frames, two types of ED devices, i.e., FED and conventional mild-carbon-steel-based ED devices, are investigated in this study. Emerging steel frames with columns of different steel grades [37] are examined in this study. Specially, the considered kernel ED devices are U-shaped strips (USSs) which are installed inside chevron braces of the steel frames.

This paper begins with a description of the working principle and representative cyclic test results of USSs. Finite element simulations are carried out based on ABAQUS software. Followed by this, the configuration and working mechanism of the brace with USSs are introduced, and its mechanical behavior is simulated. The hysteresis behavior of the braces is also simulated via the nonlinear finite element program OpenSEES [38] to facilitate system-level analysis, where necessary material parameters are calibrated. Finally, a system-level analysis is conducted to investigate the seismic response of the proposed systems under different hazard levels. Limitations and future works are also discussed.

Fe-SMA-based USS

Working principle of USS

In practice, USSs (as shown in Fig. 3) can be installed in the space between the beam and the top of chevron braces in building structures or between the deck and the top of the piers in bridges [39]. In these typical applications, the USSs serve as multi-axial ED devices since they could deform in any direction when structures are excited by earthquakes. Accordingly, the deformation can be categorized into in-plane and out-of-plane deformation modes, as shown in Fig. 4. In the present study, the USSs

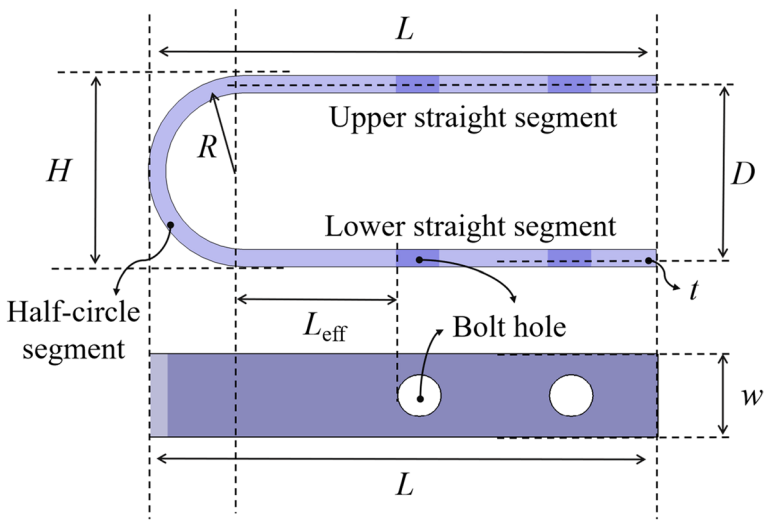

Fig. 3 Illustration of a USS

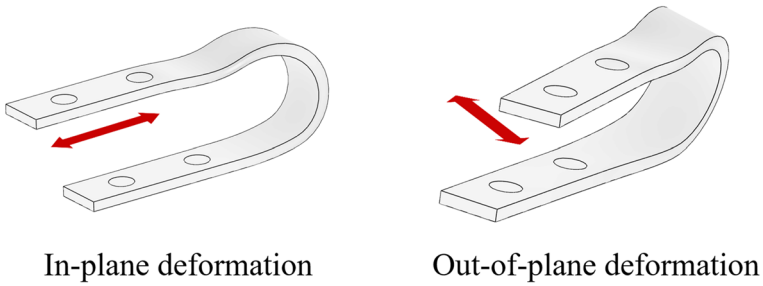

Fig. 4 Deformation modes of a USS

are assumed to be installed in the inverted-V-type braces and are designed to be deformed in an in-plane mode.

As illustrated in Fig. 3, a USS can be divided into three segments, i.e., the upper straight segment, the half-circle segment and lower straight segment. The key geometric parameters of a typical USS include the length (L) of the upper and lower straight segment, internal radius (R) of the half-circle segment, the width (w), the thickness (t) and the height ($H=2R+t$) of the USS. When the USS works, its upper and lower straight segments deform in two opposite directions, and the straight segment and half-circle segment are warped and straightened alternately under cyclic loading. The deformation mode of a USS is usually deemed as a 'rolling-bending' motion mode, that is, the two plastic zones/hinges (see Fig. 5) moves along the USS, through which the input energy is dissipated.

Theoretically, only the bending moment effect is considered for establishing the formulation of USS's damping force, and the axial and/or shear deformation effects can be ignored [40]. Assuming that the deformation of the USS concentrates on the two plastic hinges (shown in Fig. 5), the theoretical damping force F_{USS} can be derived from the conservation of energy:

$$F_{USS} \times \delta_p = 2 \times M_p \times \theta_p \tag{1}$$

where M_p, θ_p and δ_p are the plastic moment, plastic rotation and plastic displacement, respectively, as shown in Fig. 5. It is suitable to assume the USS as a curved beam, thus the plastic moment M_p can be expressed as:

$$M_p = \frac{w \times t^2 \times \sigma_p}{4} \tag{2}$$

where σ_p is the plastic stress of the USS.

The relationship between the plastic rotation and the plastic displacement can be theoretically expressed as:

$$\delta_p \approx 2 \times R \times \theta_p \tag{3}$$

The 'yield' force $F_{USS,y}$ of the USS can be calculated by substituting Eqs. 2 and 3 into Eq. 1:

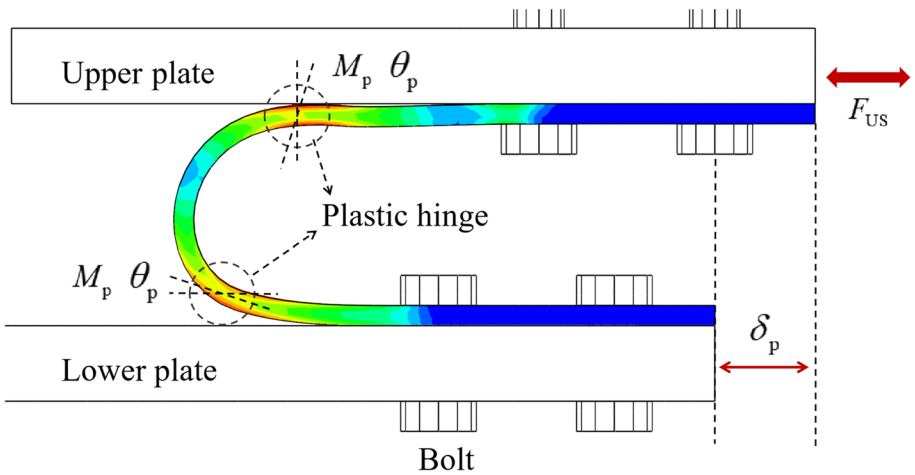

Fig. 5 Illustration for working principle of USS

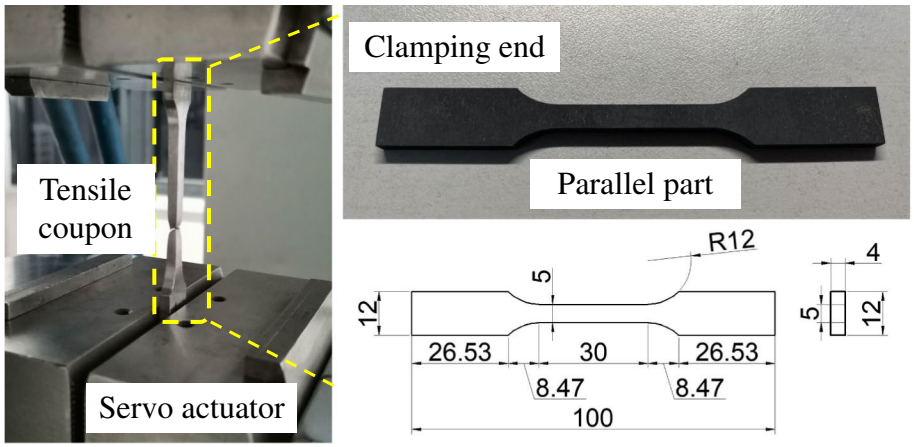

Fig. 6 Geometry of the Fe-SMA tensile-test coupon and test set-up

$$F_{\mathrm{USS},y} = \frac{2 \times M_{\mathrm{p}} \times \theta_{\mathrm{p}}}{\delta_{\mathrm{p}}} = \frac{M_{\mathrm{p}}}{R} = \frac{\sigma_y \times w \times t^2}{4 \times R} \tag{4}$$

where σ_{y} is the yield stress of the USS. It can be seen that the width, the thickness, and the radius of the half-circle segment determine the damping force of the USS. In the following subsection, the USSs were designed with varying thicknesses and radii, whereas the width is kept identical for all specimens.

Experimental study

Tension coupon tests were conducted firstly to investigate the basic mechanical properties of Fe-SMA. The chemical composition of the considered material was Fe-17Mn-5Si-10Cr-5Ni (wt%), which has been proven to possess outstanding LCF resistance [33, 34]. A detailed description of the production process of the Fe-SMA can be found in [30, 34]. The Fe-SMA was received in the form of plate, which was further manufactured to the specified geometric shapes for monotonic tension test. The monotonic test was conducted on an MTS electro-hydraulic servo actuator with a maximum force of 250 kN. A 25-mm gauge length extensometer was used to monitor and control the loading process. The configuration of the monotonic tension coupon, along with the test set-up, is illustrated in Fig. 6.

Followed by the material test, a series of proof-of-concept experiments on Fe-SMA-based USS (Fe-SMA-USS) specimens were conducted. The Fe-SMA-USSs were ordered from the same supplier. The Fe-SMA raw plates were processed by surface grinding, wire cutting, drilling, cold-bending, heat setting treatment and finally deburring to form into the shape of Fe-SMA-USS. For comparison, a batch of mild-carbon steel Q235 was also ordered for manufacturing USS specimens, namely, Q235-USS. Cyclic tests were carried out and a displacement-controlled incremental loading protocol was applied with a displacement interval equal to Δ=5mm. The loading began with two cycles each at Δ, 2Δ, 3Δ, 4Δ, 5Δ, 6Δ, 7Δ, and the cyclic loading was continued at the last displacement amplitude until fracture (see Fig. 7). The tests were conducted under quasi-static cyclic loading condition with a loading rate of 2 mm/s. It is noteworthy that a steel frame (see Fig. 8) was specially designed for the cyclic loading test of the USS specimens. When testing, the upper clamping end of the steel frame was fixed while the lower clamping end moved, making the USS specimens deform in parallel. The effective length L_{eff} may be defined as the length between the hole edge and end of the half-circle segment (as shown in Fig. 3). For clarification, the specimens were labeled by material type, i.e., 'F' for Fe-SMA and 'Q' for

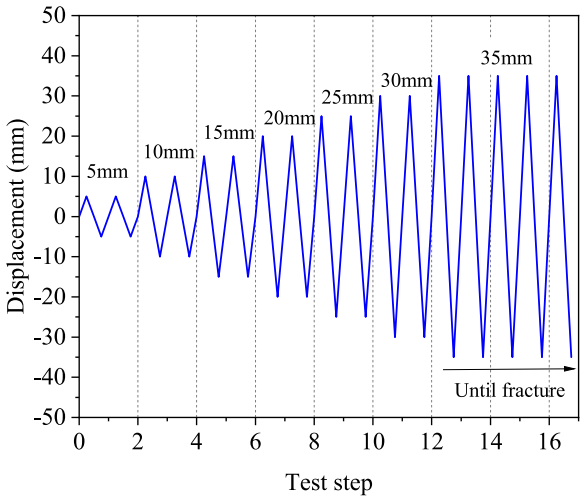

Fig. 7 Loading protocol for USS specimen

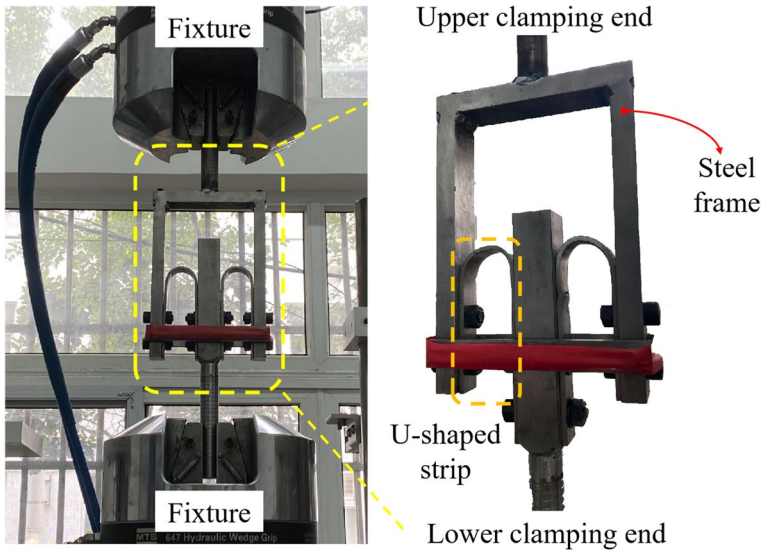

Fig. 8 Test setup for USS and specially-designed steel frame

Table 1 Measured geometrical dimensions of the USS specimens

Specimen	Code	*w* /mm	L_{eff} /mm	*t* /mm	*R* /mm
Fe-SMA-USS	F-19–6-35	19.95	35.00	5.47	19.26
	F-20–4-35	19.91	35.00	3.92	20.04
	F-20–4-50	19.93	55.00	3.93	20.04
Q235-USS	Q-19–6-35	19.96	35.00	5.37	19.32
	Q-20–4-35	19.94	35.00	4.03	19.98
	Q-20–4-50	19.96	55.00	4.00	20.00

Table 2 Mechanical properties of different metals under monotonic loading

Metal	*E* / GPa	f_y /MPa	f_u / MPa	ε_u / %	ε_f / %
Fe-SMA	180	248	695	59.21	63.44
Mild-carbon steel Q235	208	264	419	24.61	38.28
Low-yield-point steel LYP225	202	246	312	36.27	47.23
High-strength-steel Q690	218	879	917	6.87	10.54

Note: *E* is the elastic modulus; f_y is the nominal yield stress ($\sigma_{0.2}$ for Fe-SMA); f_u is the ultimate stress; ε_u is the strain corresponding to ultimate stress; ε_f is the strain corresponding to the total-fracture

Q235, followed by '*R*-*t*-L_{eff}' according to their design geometries. The measured geometrical dimensions of the USS specimens are listed in Table 1.

Test results and discussion

Material test result

The monotonic engineering stress–strain curve of the investigated Fe-SMA, along with that of some typical structural steel (i.e., low-yield-point steel LYP225, mild-carbon steel Q235 and high-strength steel Q690), has been plotted in Fig. 2, and the corresponding mechanical properties are summarized in Table 2. It can be seen that the ductility property of Fe-SMA is outstanding, with a fracture strain of more than 60%. This strain value is even larger than that of the widely-used low-yield point energy-dissipation material LYP225. Figure 9 shows a dimple-featured fractography for the fractured surface of the Fe-SMA monotonic tensile coupon, indicating a ductile fracture mode characterized by Fe-SMA. Compared with other structural steels plotted in Fig. 2, there is no yield plateau observed for Fe-SMA, thus its nominal yield stress is defined as the stress corresponding to the 0.2% offset strain, i.e., $\sigma_{0.2}$. It can be seen that the nominal yield strength of the Fe-SMA is comparable with that of Q235 and LYP225. On the other hand, a strong post-yield strain hardening behavior is observed for Fe-SMA, which is different from other metals.

Hysteresis behavior of USSs

The number of cycles to failure of the Fe-SMA USSs and Q235-USSs is listed in Table 3. The fatigue lives of the Fe-SMA-USSs are on average about 5 times of those of the Q235-USSs. The fatigue life of the 19–6-35 series specimens is about half of that of the 20–4-35 series, whereas a small difference is observed for the fatigue life between the 20–4-35 series and 20–4-50 series specimens, indicating that *R* and *t* may have a more significant effect on the fatigue life than L_{eff}. This phenomenon can be explained by Fig. 10 which shows

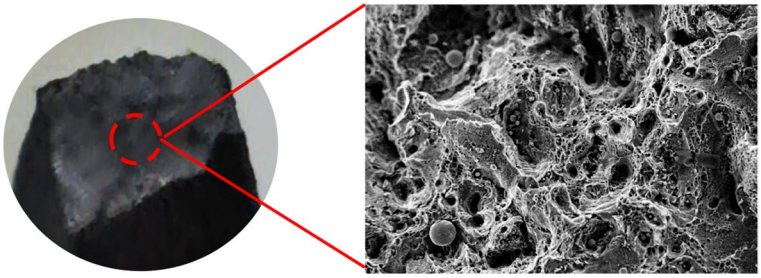

Fig. 9 Fractography of Fe-SMA monotonic tensile coupon

Table 3 Fatigue lives of the tested USS specimens

Specimen	Numbers of cycles to failure
F-19–6-35	108
F-20–4-35	200
F-20–4-50	228
Q-19–6-35	25
Q-20–4-35	41
Q-20–4-50	41

the contour of equivalent plastic strain (i.e., PEEQ in ABAQUS) of the studied USSs at the same displacement. Compared with the 20–4-35 series and 20–4-50 series USSs, the 19–6-35 series USS with a lower *R/t* ratio exhibits a larger plastic strain accumulated in the region of the inner surface of the yielding zone. This indicates that it takes less displacement (or the number of loading cycles) for the 19–6-35 series USS to accumulate the local plastic strain to the fracture threshold value than the other two series USSs with higher *R/t* ratios. Once the crack initiates, the crack propagates quickly and only a few displacement/cycles occurs at final failure. It is also of interest to observe that a longer L_{eff} provides more a controlled accumulation of plastic strain under the same loading conditions, as shown in Fig. 10b-c, suggesting that a longer fatigue life may be achieved with an increased L_{eff}. For example, the fatigue lives of specimens F-20–4-35 and F-20–4-50 are 200 cycles and 228 cycles, respectively, as listed in Table 3.

The typical hysteresis responses of the USSs under in-plane loading are plotted in Fig. 11. A symmetric load-deformation behavior is observed. It can be seen that the hysteresis loops (see Fig. 11) and the positive peak forces (see Fig. 12a) of 20–4-50 and 20–4-35 series specimens are almost the same, indicating that the length of straight segment has no influence on the mechanical behavior of the USS. In practice, the length of the straight segment should not be too short since this parameter controls the deformation capacity of USS.

The typical skeleton curves that link the tip of the hysteresis loops of specimens F-19–6-35 and Q-19–6-35 are plotted in Fig. 11. It can be seen that the post-yield stiffness of the skeleton curve of Fe-SMA-USS is higher than that of Q235-USS. A dimensionless index, i.e., equivalent viscous damping ratio (EVD), is employed to represent the energy-dissipation capacity, as expressed as [41]:

$$EVD = \frac{W_D}{4\pi W_E} \tag{5}$$

where W_D is the absolute area enclosed by the hysteretic loop per cycle; and W_E is the energy stored in

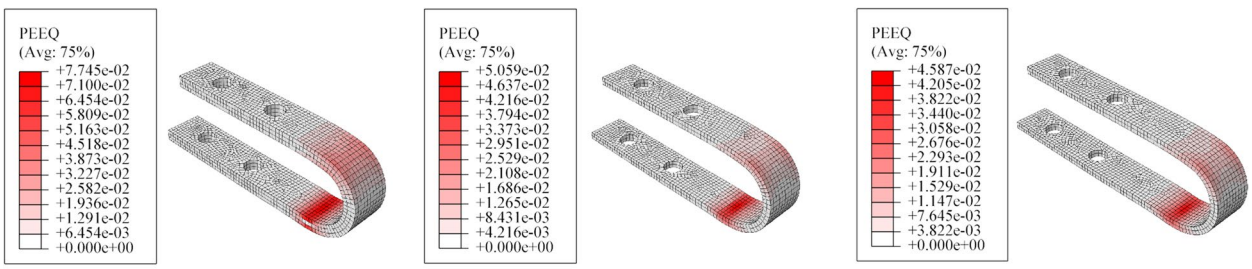

Fig. 10 Contour of the equivalent plastic strain of USSs of **a** 19–6-35 series, R/t = 3.17; **b** 20–4-35 series, R/t = 5; and **c** 20–4-50 series, R/t = 5. With 15 mm in-plane displacement applied

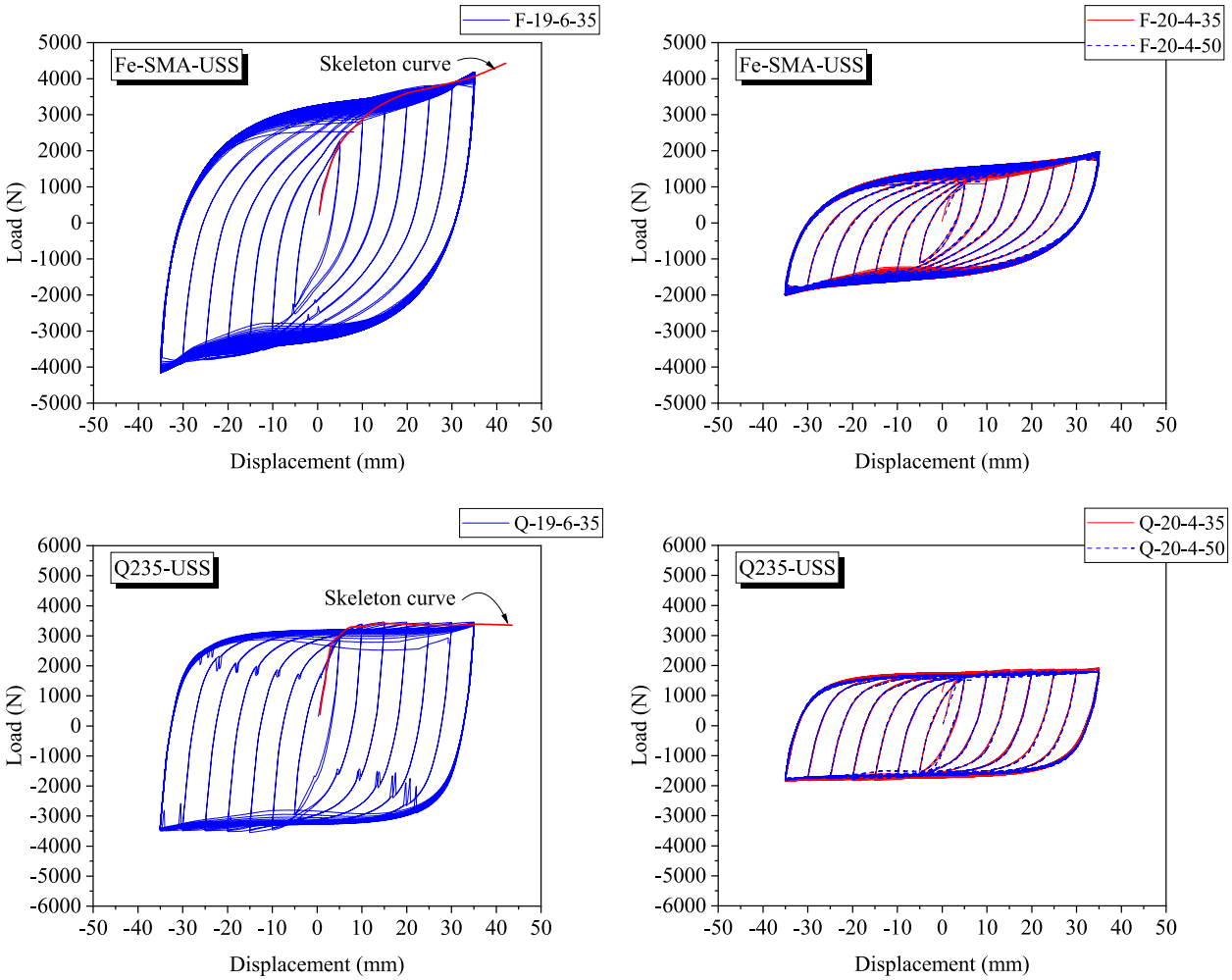

Fig. 11 Cyclic test results of USS specimens

the corresponding linear system. The calculated EVD results of the USS specimens are plotted in Fig. 12b. The EVDs of the Fe-SMA-USSs are on average 15% lower than those of the Q235-USSs because the shape of the hysteretic loops of Fe-SMA-USS is not as plump as that of Q235-USS. This is mainly due to the higher peak force and pseudo-elasticity phenomenon exhibited by Fe-SMA. The accumulated energy-dissipation capacity of the two types of USSs are further compared in Fig. 13. It can be seen that although the single cycle energy dissipation of Fe-SMA-USSs is lower that of their Q235 counterparts, the total energy dissipation of the Fe-SMA-USSs is about 5 times that of the Q235-USSs. Again, this phenomenon results from the extraordinary long LCF life of the Fe-SMA-USSs (as summarized in Table 3). Another interesting finding is that the peak forces of the Fe-SMA-USSs are kept stable until a sudden load-drop occurred, whereas the peak forces of the Q235-USS decreases slowly before total fracture, indicating that the crack propagation pattern and the fracture mode may be different between these two types of USSs.

Finite element simulation of USS

Finite element simulation of the USS was conducted to serve as a validation study for the follow-up system-level analysis considering USS-based energy-dissipative braces (hereafter referred to as brace). The simulation work was performed with ABAQUS software [42]. As shown in Fig. 14, a 3D finite element model was established, where the C3D8R solid elements which consider reduced integration and hourglass control were employed. Part of the specially-designed frame was modeled as rigid body since the frame is essentially elastic. The 'preload' command was used to simulate the preload condition of the

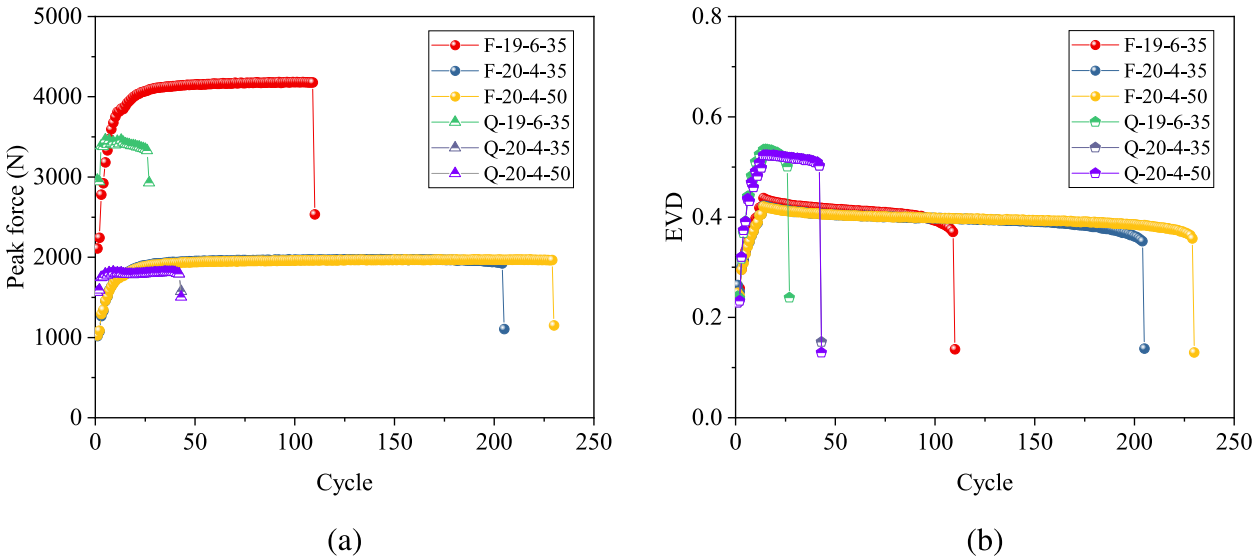

Fig. 12 **a** Peak force; and **b** EVD value of USS specimens per cycle

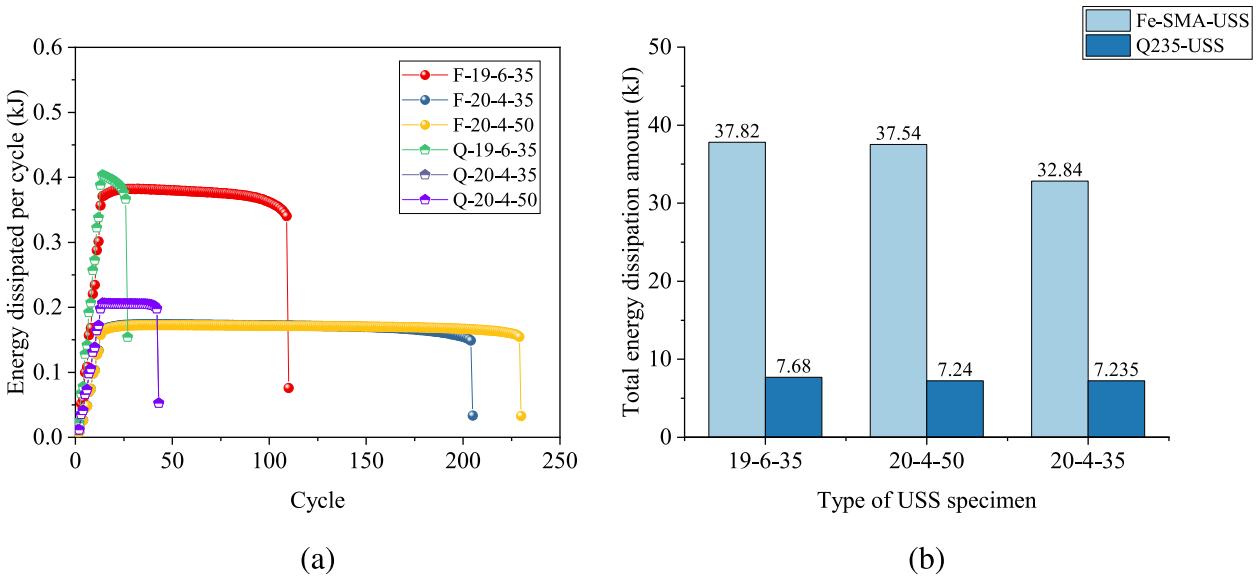

Fig. 13 **a** Energy dissipation amount per cycle; and **b** Total energy dissipation amount of USS specimens

high-strength bolts. The interaction among the bolts were modelled via 'hard contact' option in the normal direction and 'penalty' friction (with a friction coefficient of 0.3) in the tangential direction. As shown in Fig. 14, two reference points (RPs) were set at the two ends of the steel frame, and the upper and lower beams of the steel frame were then coupled to the RPs. The displacement-controlled in-plane loading (the loading protocol was consistent with the test program) was applied at the lower beam while a completely fix boundary condition was applied at the upper one.

A combined isotropic-kinematic hardening rule [43], which has been proven to be efficient in describing the cyclic response of the metal under reverse loading, is adopted. The inelastic behavior is defined by the change of yield surface f and is defined as:

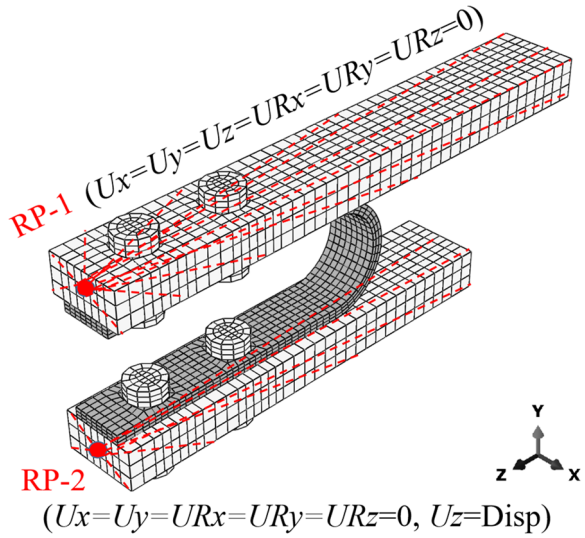

Fig. 14 Meshed finite element model and boundary conditions of USS

$$f = \sqrt{\frac{3}{2}(\boldsymbol{S}_k - \boldsymbol{\alpha}_k)(\boldsymbol{S}_k - \boldsymbol{\alpha}_k)} - \sigma^0 \tag{6}$$

where $\boldsymbol{S}_k$ is the deviatoric stress tensor; $\boldsymbol{\alpha}_k$ is the backstress vector; σ^0 is the yield stress.

The kinematic hardening rule is often described in terms of backstress vector α, which can be described as [43]:

$$\alpha = \sum_{k=1}^{B} \alpha_k \tag{7}$$

$$d\boldsymbol{\alpha}_k = \frac{C_k}{\sigma^0}(\boldsymbol{\sigma} - \boldsymbol{\alpha})d\varepsilon^p - \gamma_k \boldsymbol{\alpha}_k \varepsilon^p \tag{8}$$

where C_k and γ_k are material parameters to be calibrated; $d\varepsilon^p$ and ε^p are the incremental and current equivalent plastic strain, respectively, where $\varepsilon^p = \sqrt{\frac{2}{3}\varepsilon^p_{ij} \cdot \varepsilon^p_{ij}}$; σ is the stress vector; B is the total number of the backstresses. It is suggested that a more accurate simulation can be achieved as the number of backstresses increases, which of course requires a greater cost in the calibration process.

The evolution of the isotropic hardening component is described by σ^0:

$$\sigma^0 = \sigma|_0 + Q_\infty\left(1 - e^{-b\varepsilon^p}\right) \tag{9}$$

where $\sigma|_0$ is the yield stress at zero plastic strain; Q_∞ is the maximum size of the yield surface; b is the rate at which the size of the yield surface changes for increasing plastic strains. The constitutive model parameters that define the hysteresis response under the tested incremental loading protocol were determined through several back-calculation processes against the experimental results. The calibrated parameters are listed in Table 4. As shown in Fig. 15, there is a good agreement between the experimental and numerical results, indicating the feasibility of the calibrated parameters for capturing the cyclic behavior of the USS specimens.

Behavior of brace in this study

Assembly and working principle of brace

The studied brace assembly is schematically shown in Fig. 16. The configuration of such brace was first proposed by Taiyari et al. [39]. The brace employed USSs as its kernel energy-dissipative elements. The brace components include the outer tube, the Z-shaped inner plate, end-plate, connection plate and tightening nuts. On one side of the brace, the connection plate was welded to the end-plate, while the end-plate was further welded to the Z-shaped inner plate. On the other side of the brace, another connection plate was welded to the outer tube. Bolt-holes were reserved in the connection angles and connection plate.

During assembly, one of the straight segments of the USS is first connected to the Z-shaped inner plate, by either fillet welding or bolting, and the other straight segment is connected to the outer tube. The entire assembly process can be prefabricated in the workshop. The brace is finally connected to the main frame by connection plates.

The working principle of the brace is demonstrated in Fig. 17. For ease of description, it is assumed that the outer tube is completely fixed. When a brace works, the inner part is 'pulled' or 'pushed' along the longitudinal direction of the brace. The relative displacement between outer tube and inner plate deforms the USSs (with an in-plane mode) which are located between them. Theoretically, the total damping force of the brace is simply provided by the USs installed in it, although there may exist some inevitable friction in practice. It is noteworthy that the number of the USs can be adjusted according to the design requirement.

Table 4 Calibrated cyclic constitutive parameters for simulating USS specimens on ABAQUS

Specimen	$\sigma\|_0$/ MPa	Q_∞/ MPa	b	C_1/ MPa	γ_1	C_2/ MPa	γ_2
Fe-SMA-USS	160	80	3.5	20,000	180	1000	0
Q235-USS	235	55	20	60,960	450	0	0

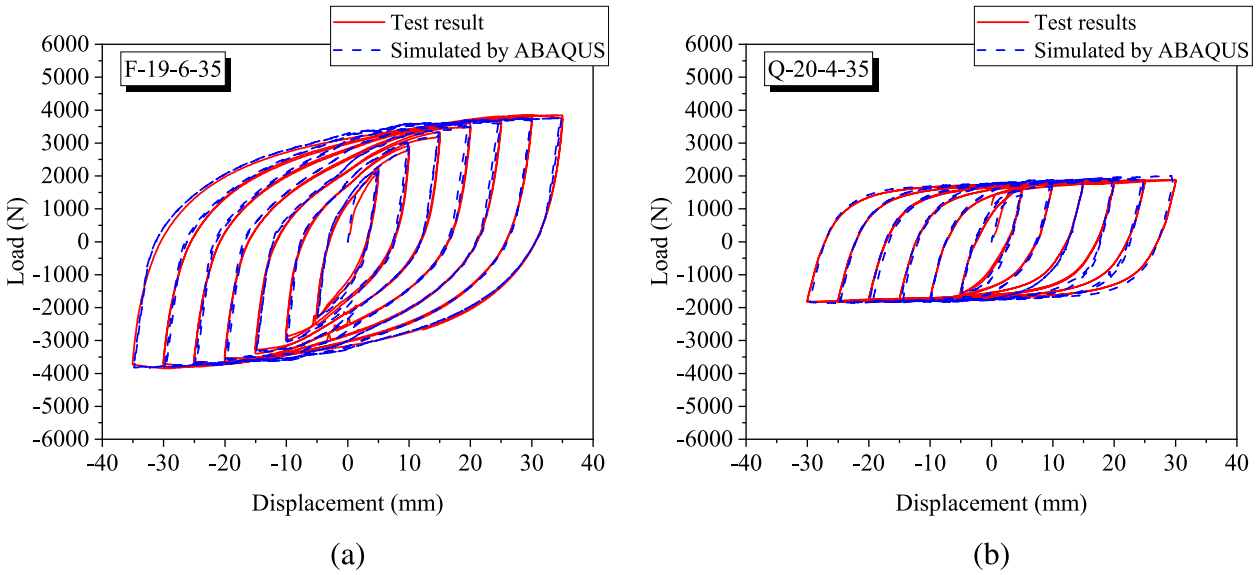

Fig. 15 Representative comparison between test results and finite element simulation result of USS specimens

Numerical modeling and parameter calibration for brace

Component-level simulation of brace was carried out. The brace was designed to be placed diagonally in a 3 m span and 3 m height frame bay, whose dimension is consistent with the prototype building in the system-level analysis which is discussed later. The Z-shaped inner plate was designed to be thick enough (30 mm in this paper) to avoid local bucking under cyclic loading. The key dimensions of the prototype brace are shown in Fig. 18. As mentioned above, the number of USSs installed in the brace can be determined according to the load demand. For the brace designed in this paper, 5 to 8 USSs are suggested with the consideration of both the space restriction and the capacity of providing necessary damping force. Table 5 gives the design information of brace considering different number of USSs. The configuration of the USS can be referenced in Figs. 16 and 18.

ABAQUS was first used to obtain the cyclic behavior of the 'full-scale' braces used in the prototype buildings. Two types of braces, i.e., brace adopting Fe-SMA-USSs (denoted as Fe-SMA-brace), and brace adopting mild-carbon-steel-based Q235-USSs (denoted as Q235-brace), were simulated. A total of six USSs were installed in each brace. The element type, the material properties as well as the interaction options for establishing the brace models are identical to the modelling method that has been validated in Section Finite element simulation of USS. The minimum mesh size is determined as 9 mm to seek balance between calculation efficiency and accuracy. Incremental loading protocol with a step interval = 30 mm is employed for the displacement-controlled loading process. The simulated hysteresis loops for the full-scale Fe-SMA-brace as well as Q235-brace are plotted in Fig. 20.

After obtaining the behavior of the individual brace through ABAQUS, the cyclic behavior of the brace is further simulated via OpenSEES [44] to facilitate system-level analysis. As shown in the right part of Fig. 19, a truss element constructed with a uniaxial material property is utilized to simulate the mechanical behavior of the brace. Owing to the multiple adjustable parameters and excellent capability of accurately capturing the hysteresis behavior, the *UVCuniaxial* material command in OpenSEES is adopt. This model is based on the Voce isotropic hardening law and the Chaboche kinematic hardening law which have been introduced above. Based on the ABAQUS results, the model parameters for analysis at system level were determined through several rounds of trial-and-error iterations to achieve a satisfied fitting agreement. The calibrated *UVCuniaxial* parameters for the Fe-SMA-brace and Q235-brace trusses are listed in Table 6. Figure 20 shows the comparison between the simulation results provided by ABAQUS-3D finite element model and that by OpenSEES-2D truss element model. It can be seen that the calibrated *UVCuniaxial* material parameters are capable of capturing the mechanical behavior of the brace simulated by truss element.

System-level analysis

Prototype buildings

A series of system-level analyses are conducted to understand the fundamental performance of the frames equipped with FED under earthquakes. The analysis

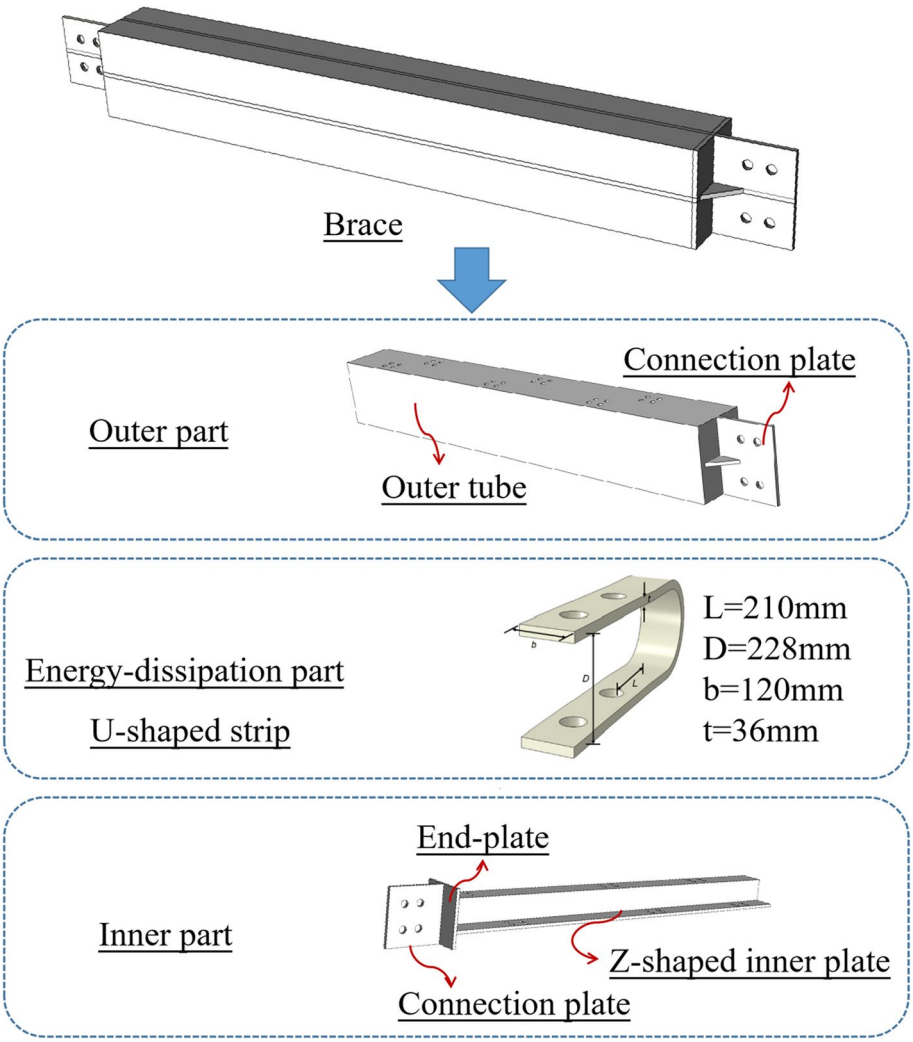

Fig. 16 Three-dimensional schematic illustration of brace

was performed on four 5-story concentrically braced prototype steel buildings with different boundary frame types and different ED systems:

1) HSSF-FED: steel frames with high-strength steel columns (Abbreviated as HSSF), and equipped with Fe-SMA-based ED system (Abbreviated as FED);
2) HSSF-ED: steel frames with high-strength steel columns, and equipped with conventional mild-steel-based ED system;
3) SF-FED: steel frames with conventional mild steel columns (Abbreviated as SF), and equipped with Fe-SMA-based ED system;
4) SF-ED: this is the most commonly used structural scheme, that is, steel frames with conventional mild steel columns and equipped with conventional mild-steel-based ED system.

In this work, the investigated Fe-SMA-brace and Q235-brace are adopted as the FED and conventional ED systems, respectively. It is noted that the nominal yield strength and the axial stiffness of the Q235-brace are comparable to those of the investigated Fe-SMA-brace, as summarized in Tables 6 and 7. In other words, the main difference in the behavior between the Q235- and Fe-SMA-brace is the strain-hardening law under cyclic loading, in addition to the difference in the unloading path.

Design and modeling of prototype buildings

Modal-response spectrum analysis is conducted to calculate the required base shear and to determine the member sizes of the main-frames. The frames are assumed to be located at a stiff soil site (site class D) in Los Angeles. The importance factor I_e, the response modification coefficient R and the deflection amplification factor C_d,

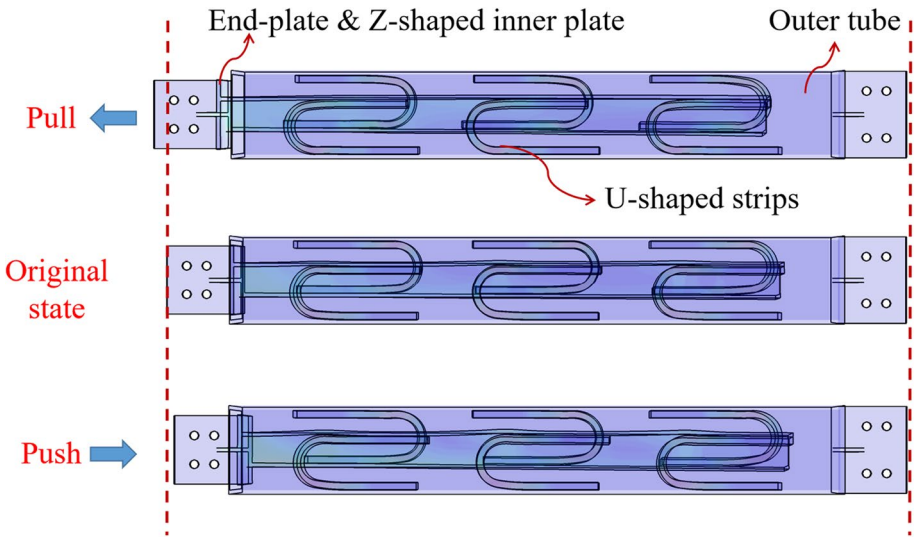

Fig. 17 Working principle of brace

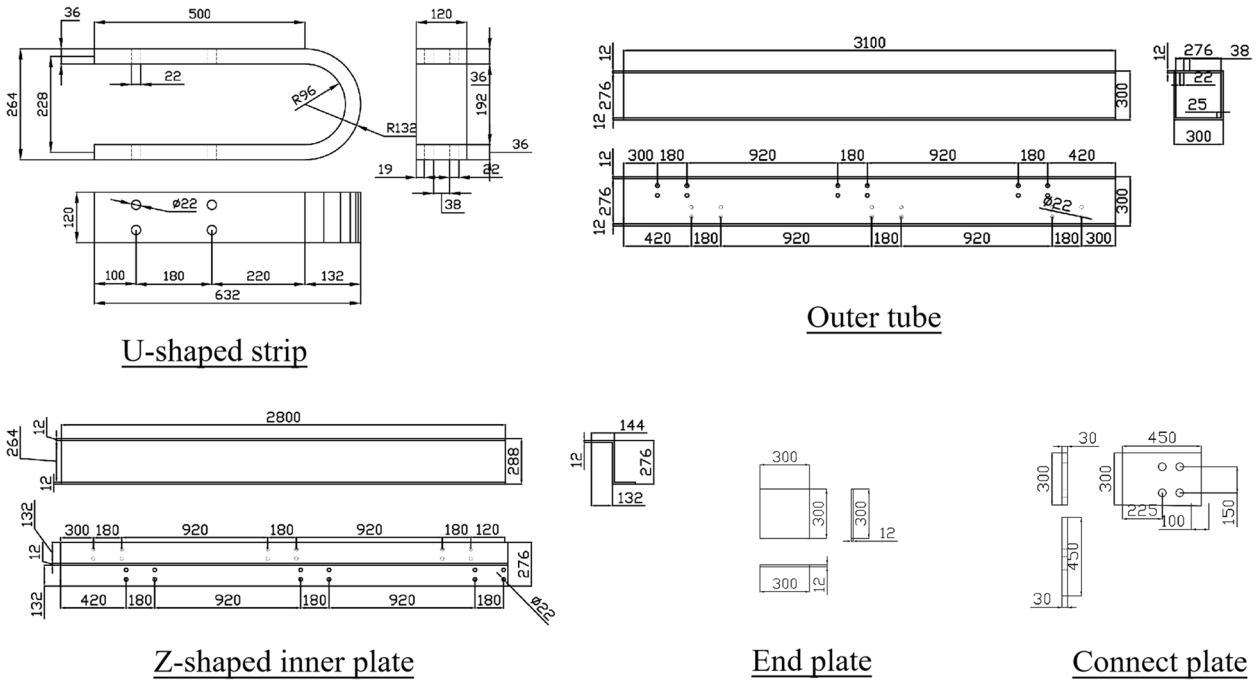

Fig. 18 Key dimensions of prototype brace (units in mm)

are taken as 1.0, 8.0, and 5.0, respectively. The design response spectral values $S_{MS} = 3/2S_{DS} = 2.064$g, and $S_{M1} = 3/2S_{D1} = 1.061$g (where g represents gravitational acceleration), are considered.

2D frames that represent half of the structures in the North–South (NS) direction are established, as shown in Fig. 21. The plan and elevation views of the buildings, together with the sizes of the main components at different stories, are listed in Table 7. All these frames are designed to have the same architectural dimensions, where the typical bay width is 9.15 m and the story height is 3.96 m. Q345 steel with a nominal yield strength of 345 MPa is adopted for the conventional steel frame columns, while Q550 steel (a class of high-strength steel) with a nominal yield strength of 550 MPa was employed for the HSSF columns. The nominal yield strength of the

Table 5 Design information of brace

Brace type	Number of USSs installed	Initial yield force of brace / kN	Spacing between USS / mm
Fe-SMA-brace	5	325	1100
	6	390	1100
	7	455	775
	8	520	775
Q235-brace	5	326	1100
	6	391	1100
	7	456	775
	8	521	775

beams for all these frames is 248 MPa. In this paper, it is preliminarily assumed that the total yield resistance of the cross-section of the high-strength steel column is equal to that of the column with normal steel. For each frame, three column sizes are used along the height. The corresponding splicing joints are located at the height of 5.79 m and 13.71 m, as represented by the black dots in Fig. 21. The braces are installed at the exterior bays of the boundary steel frames with a chevron arrangement. The arrangement of the braces is identical for all the considered frames. The detailed information of the braces is listed in Table 7. Subsequently, nonlinear response history procedure conforming to the ASCE 7–16 [45] is conducted to doublecheck whether the inter-story drift responses are within the codified threshold, i.e., 2.0% under the design-based earthquake (DBE).

Nonlinear dynamic analysis is carried out with the OpenSEES platform [44]. Pin connections are assumed for the beam-to-column connections located at the rightmost external column (see Fig. 21) and rigid connections are assumed for the remaining beam-to-column connections. The bases of the columns are fixed to the ground. Displacement-Based Beam-Column Element is used to simulate the boundary frame members, and *Steel01* material with idealized kinematic hardening property is utilized. The gravity load is properly applied to the frame through an axially rigid leaning column to account for the global $P-\Delta$ effect. The leaning column is comprised of pin-to-pin segment and is modelled by *EqualDOF* command. The braces are simulated by truss elements and the corresponding key parameters are taken from Tables 6 and 7. The first three fundamental periods of vibration of the investigated frames are listed in Table 8. A Rayleigh damping ratio of 5% is assumed for the first three modes. In the numerical simulation, the Newton algorithm and Newmark integration method are employed for transient analysis.

Ground motions

Nonlinear time-history analysis was performed to evaluate the seismic behavior of the considered frames under earthquake ground motions. A group of twenty ground motion records were adopted from the PEER NGA database. These ground motions were selected and scaled to

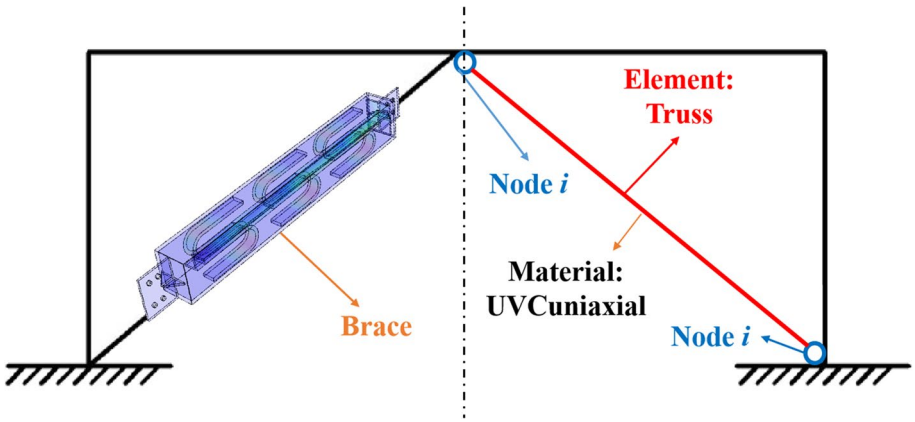

Fig. 19 Simulation for brace based on ABAQUS (left part) and OpenSEES (right part) platforms

Table 6 Calibrated *UVCuniaxial* parameters for the brace truss

Brace type	E/ GPa	f_y/ MPa	Q_{inf}/ MPa	b	N	C_1/ MPa	γ_1	C_2/ MPa	γ_2	D_{inf}/ MPa	a
Fe-SMA-brace	180	272	14	4.2	2	12,435	94.04	10,434	62.93	0	1
Q235-brace	200	273	23	9.2	2	14,527	154.04	4325	122.93	0	1

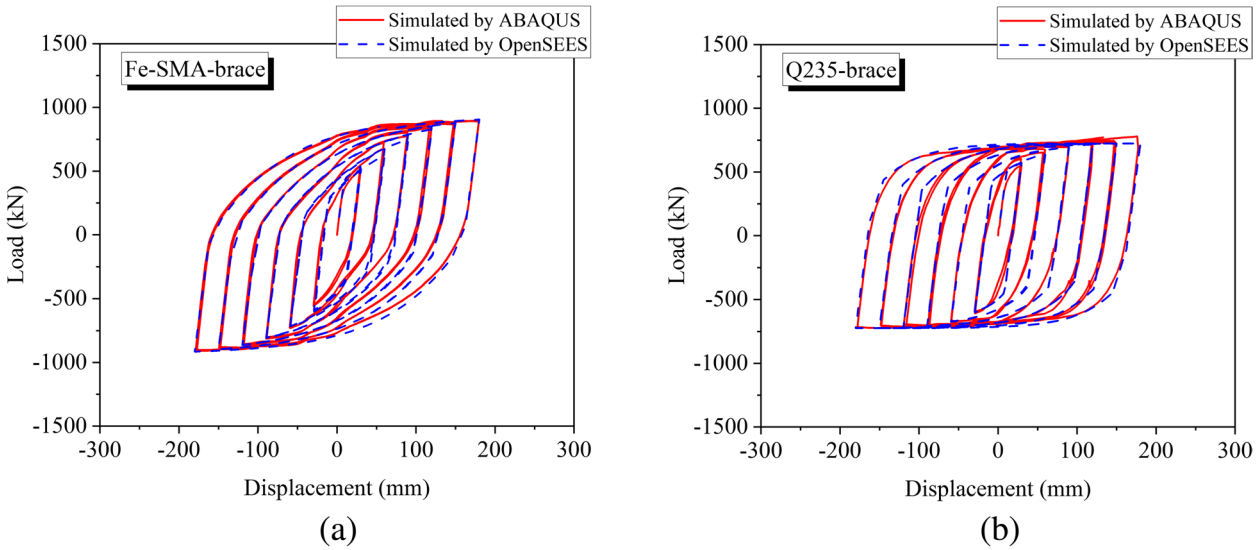

Fig. 20 Comparison of finite element simulation results simulated by ABAQUS and OpenSEES platforms

Table 7 Basic information of studied frames

Story	SF		HSSF			brace	
	Column	Beam	Column	Beam	Number of USSs installed in each brace	Number of braces in each story	Each truss area (mm^2)
1	W14X257	W30X108	W14X159	W30X108	8	4	1912
2	W14X257/ W14X211	W30X108	W14X159/ W14X132	W30X108	8	4	1912
3	W14X211	W24X84	W14X132	W24X84	8	4	1912
4	W14X211/ W14X176	W21X68	W14X132/ W14X109	W21X68	6	4	1434
5	W14X176	W21X68	W14X109	W21X68	6	4	1434

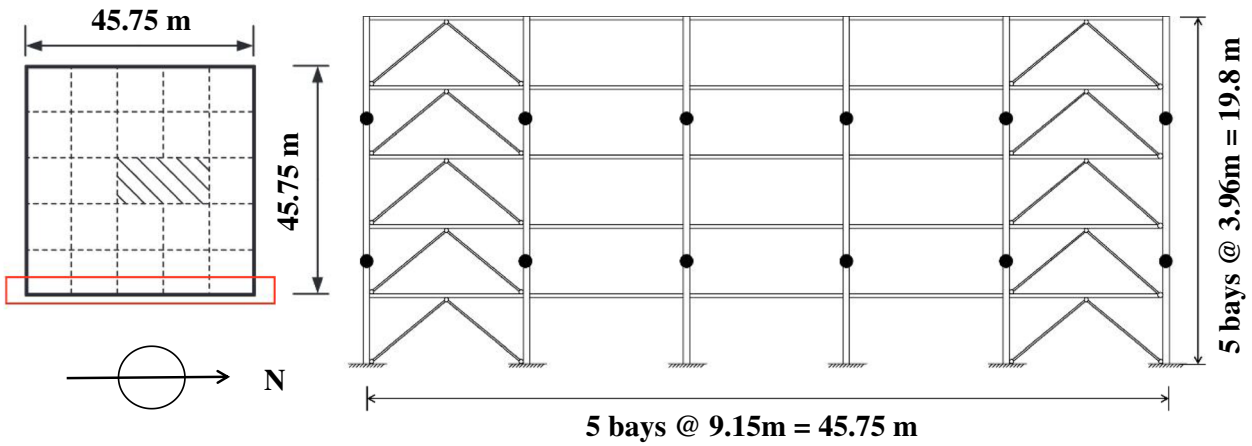

Fig. 21 Illustration of 5-story prototype building

Table 8 Natural vibration period of investigated frames

Frame type	T_1 / s	T_2 / s	T_3 / s
HSSF-FED	1.242	0.427	0.241
HSSF-ED	1.204	0.415	0.235
SF-FED	1.171	0.399	0.220
SF-ED	1.136	0.389	0.218

T_1, T_2 and T_3 are the 1st, 2nd and 3rd fundamental period of the frames

the design-basis earthquakes (DBE, 10% probability of exceedance in 50 years) level as well as the maximum considered earthquake (MCE, 2% probability of exceedance in 50 years) level according to ASCE 7–16 [45]. The information of the selected ground motions is listed in Table 9. These records were scaled using the mean square error method so that the mean response spectrum can match the design spectrum as much as possible over the range between 0.2 T_1 and 1.5 T_1, where T_1 is the fundamental period of frame. Figure 22 shows the 5%-damped linearly elastic response spectra S_a for each ground motion record. In order to obtain the permanent deformation of the frame after earthquake, an extra 10-s time-history with zero acceleration amplitude was appended to the end of each ground motion so that the vibration decays out completely.

Structural performance

Peak inter-story drift

The mean peak inter-story drift ratios (PIDs) of the frames are shown in Fig. 23a. The results show that the PIDs of the HSSFs are slightly larger than that of the SFs under both hazard levels. The reason could be that the cross-sectional area of the high-strength steel column is reduced compared with that of the normal mild steel column, making the stiffness of the HSSF lower than that of the SF, noting that higher PIDs are often exhibited in structural frames with lower stiffness. It is also seen from Fig. 23a that the application of FED tends to slightly increase the PID response of the frames compared with those equipped with conventional ED system. Again, this phenomenon is partially attributed to the slightly lower elastic stiffness of FED (see Table 6). Generally speaking, the influence of the two types of ED systems on the PID response is limited and may be negligible.

Residual inter-story drift

The mean residual inter-story drift ratios (RIDs) of the investigated frames under different hazard levels are presented in Fig. 23b. In order to assess the damage conditions of the post-earthquake structures and associated potential economic loss, several damage states (DS) are specified in FEMA P-58 [46]. Under DS1 level,

Table 9 Earthquake records information

No	Earthquake name	Year	Station	PGV (cm/s)	PGA (g)
FF-1	Imperial Valley-02	1940	El Centro Array #9	25.156	0.254
FF-2	Borrego	1942	El Centro Array #9	6.200	0.066
FF-3	Kern County	1952	LA—Hollywood Stor FF	8.623	0.041
FF-4	Kern County	1952	Pasadena—CIT Athenaeum	5.874	0.048
FF-5	Kern County	1952	Santa Barbara Courthouse	11.406	0.090
FF-6	Kern County	1952	Taft Lincoln School	15.222	0.145
FF-7	Northern Calif-03	1954	Ferndale City Hall	34.784	0.162
FF-8	Hollister-01	1961	Hollister City Hall	8.011	0.059
FF-9	Parkfield	1966	Cholame—Shandon Array #12	5.391	0.060
FF-10	Parkfield	1966	Cholame—Shandon Array #5	25.038	0.444
FF-11	Parkfield	1966	Cholame—Shandon Array #8	10.565	0.248
FF-12	Borrego Mtn	1968	El Centro Array #9	19.852	0.133
FF-13	San Fernando	1971	LA—Hollywood Stor FF	21.707	0.225
FF-14	San Fernando	1971	Lake Hughes #1	16.210	0.151
FF-15	San Fernando	1971	Palmdale Fire Station	11.511	0.103
FF-16	San Fernando	1971	Pasadena—CIT Athenaeum	7.633	0.087
FF-17	San Fernando	1971	Whittier Narrows Dam	10.130	0.079
FF-18	Managua_ Nicaragua-01	1972	Managua_ ESSO	23.301	0.372
FF-19	Managua_ Nicaragua-02	1972	Managua_ ESSO	18.838	0.150
FF-20	Point Mugu	1973	Port Hueneme	9.392	0.128

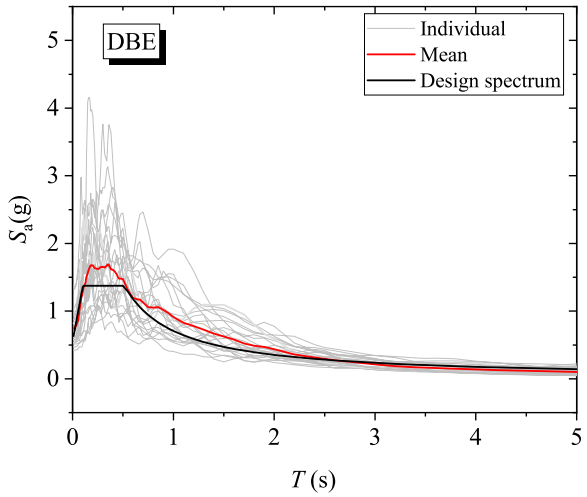

Fig. 22 Response spectrum for DBE level

it is considered that the structures only need minor post-earthquake retrofit, or only needs to repair some non-structural components. Under DS2 level, necessary economic structural maintenance is required and the structural stability is reduced to some extent. The RID thresholds for DS1 and DS2 are 0.2% and 0.5%, respectively. It can be seen that under the DBE level, all the frames meet the DS1 requirement. However, when the frames are under the MCE, only the HSSF-FED can effectively control the frames within the DS2 limit, which confirms the effectiveness of the proposed HSSF-FED in controlling RID. Compared with conventional SF-ED systems, the maximum RID of HSSF-FED is reduced by 45%. The pronounced RID control capability is benefited from the combined advantages of the high-strength steel column's extended elastic range and FED's high post-yield stiffness and pseudo-elasticity, both offering tendency of re-centering during dynamic shakedown.

Absolute floor acceleration

The height-wise mean absolute floor acceleration (PFA) distributions of the considered four types of frames are shown in Fig. 23c. Past earthquakes reveal that injuries, fatalities, repair costs and disruption time related to failure of non-structural components due to large PFA could far exceed those associated with structural damages [47]. The SF-FED has the maximum mean PFA response among the four frames under both the DBE and MCE. Compared with structure SF-ED, the maximum PFA of structure SF-FED is increased by 15% under the DBE and by 24% under the MCE. This is mainly due to the high post-yield stiffness of the Fe-SMA-brace. It is reported that metal damper with a lower cyclic hardening property tends to reduce the absolute floor

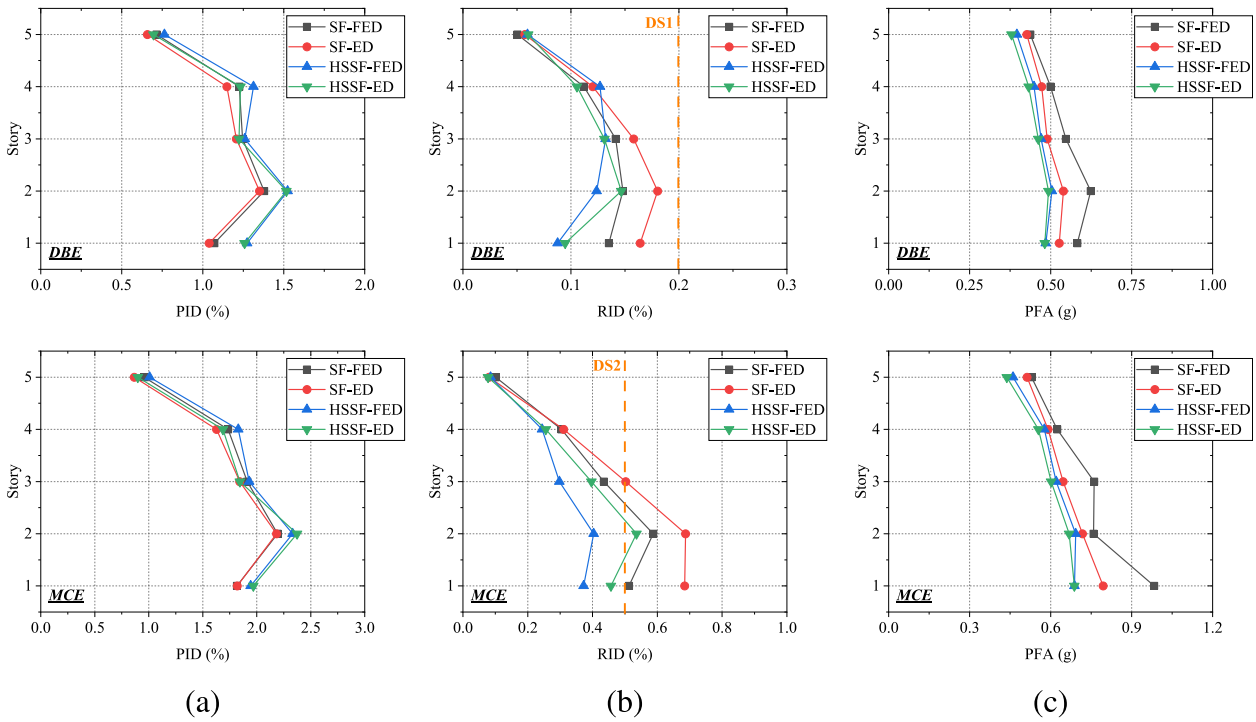

Fig. 23 Mean seismic responses of structures: **a** Peak inter-story drift (PID), **b** Residual inter-story drift (RID) and **c** Absolute floor acceleration (PFA)

acceleration demands [28]. On the other hand, the mean PFA of the HSSF-FED is evidently decreased compared with that of the SF-FED system due to the more flexible behavior of the former.

Case study

Case studies were further conducted. The scaled ground motion FF-7 and FF-12 at the MCE level was employed and the corresponding acceleration-time history record is plotted in Fig. 24. Figure 25 shows the roof drift time-history results of the four frames. The comparison between FED and conventional ED is first made, as shown in Fig. 25a, where the former can effectively control the roof drift ratio for different types of steel frames. This phenomenon is attributed to the higher post-yield stiffness and pseudo-elasticity behavior of FED which provides a stronger re-centering tendency. Figure 25b compares the roof drift response of conventional SF and HSSF equipped with conventional ED devices. It is confirmed that the residual roof drift ratio is reduced in the HSSF where the high-strength steel columns provide larger elastic deformation and hence increased elastic restoring action. A relatively larger peak roof drift is observed for the HSSFs, phenomenon which has been explained in Sect. 4.4.1. When focus is paid on the performance of HSSF-FED with the comparison of conventional SF-ED, significant difference is observed between them. A better roof drift control capacity is achieved for HSSF-FED, with the residual roof drift ratio reduced by 75.9% and 81.05% under FF-7 and FF-12 ground motions, respectively. The post-earthquake residual roof drift is almost pull-backed to the original position in HSSF-FED system, as shown in Fig. 25c. Such results strongly indicate that the newly emerged HSSF-FED has an outstanding advantage in controlling residual drift compared with conventional yielding structural systems.

Conclusions

Two types of steel frames (conventional steel frame and high-strength-steel frame) equipped with various energy-dissipation devices were analyzed. U-shaped strip-based braces served as the kernel member in this investigation. The material behavior of Fe-SMA was first investigated, followed by the discussion of Fe-SMA-USSs. The cyclic behavior of the Fe-SMA-brace was then simulated. For comparison, braces with identical geometry but fabricated by conventional mild-carbon steel Q235 (Q235-brace) were also studied. System-level analysis was performed to reveal the influence of different factors on structural performances of practical concern. The main findings and conclusions are summarized as follows.

1) Fe-SMA has higher post-yield stiffness and higher ductility compared with normal steel. The outstanding low cycle fatigue life as well as satisfied energy dissipation capacity make Fe-SMA a strong candidate in the field of seismic engineering.
2) The cyclic tests on Fe-SMA U-shaped strips show that the single-cycle energy-dissipation capacity of Fe-SMA-based devices is comparable to conventional mild-steel-based energy-dissipation devices. While the EVD of the Fe-SMA U-shaped strips is lower than that of the mild-steel ones due to the higher peak strength and mild pseudo-elastic behavior of the former, the total energy dissipation of Fe-SMA U-shaped strips prior to failure is significantly more than that of their mild-steel counterparts owing to the extraordinary low cycle fatigue life of Fe-SMA.
3) System-level analysis shows that the HSSF-FED exhibits the most satisfied performance in limiting RID, with the RID index effectively controlled within the DS2 threshold under the MCE hazard level. The HSSF's inherently large elastic range and Fe-SMA's relatively high post-yield stiffness and mild pseudo-elasticity behavior are both responsible for this phenomenon.

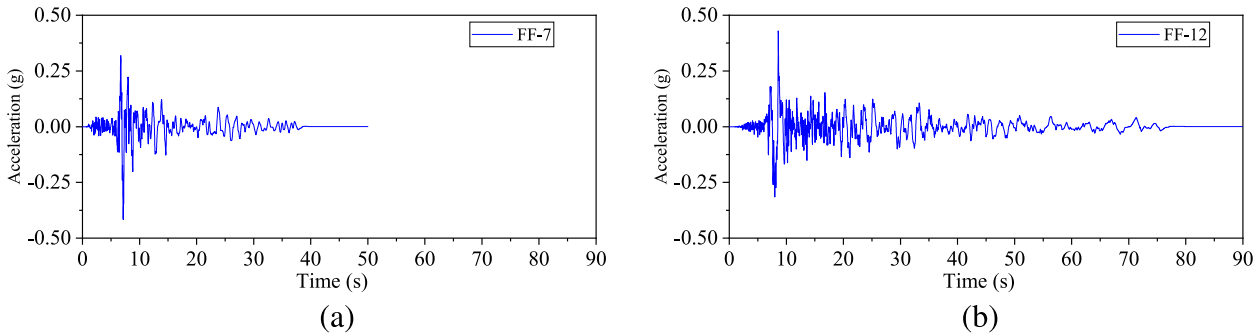

Fig. 24 Acceleration time history of (**a**) FF-7 and (**b**) FF-12 ground motion records (scaled to the MCE level)

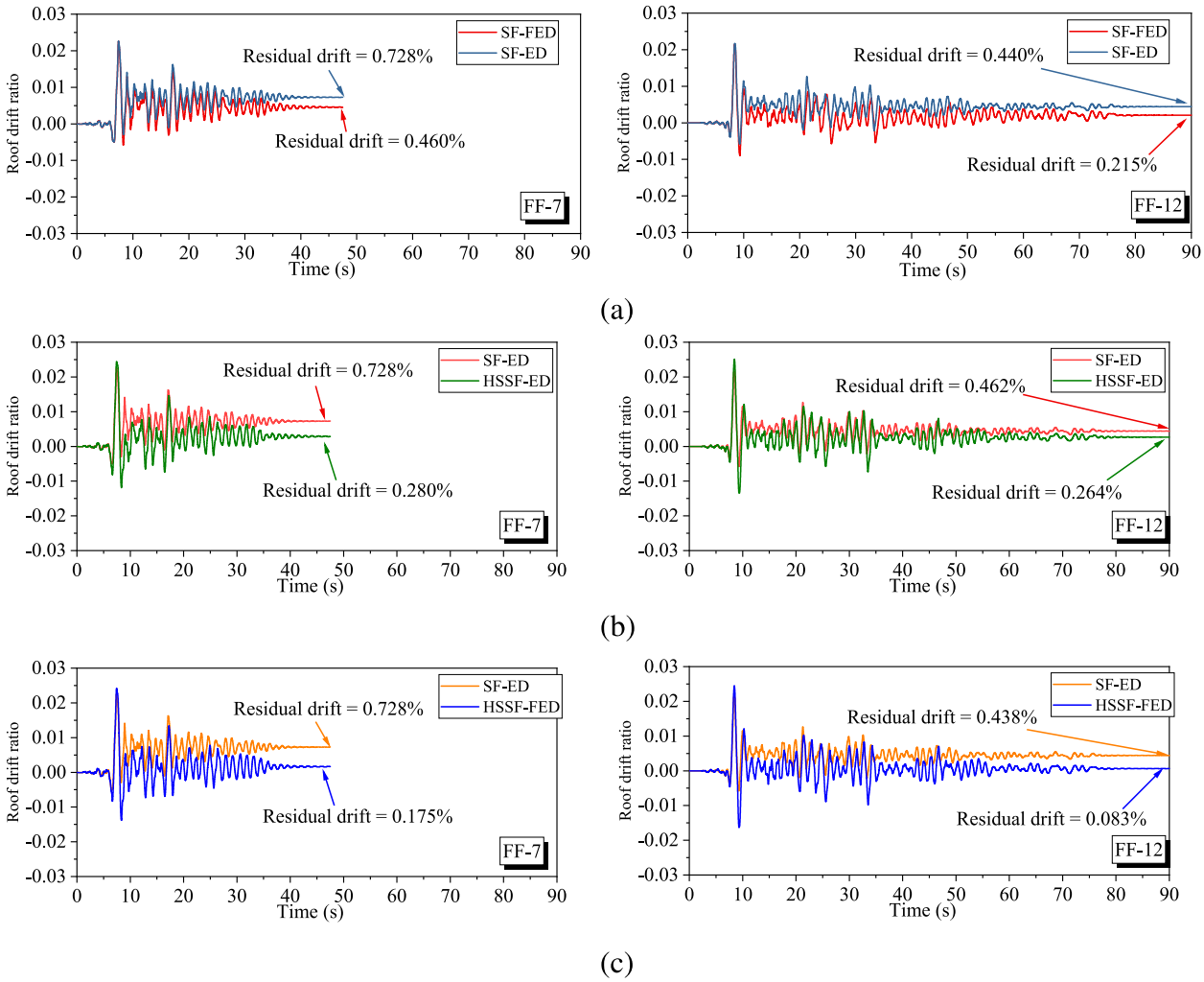

Fig. 25 Roof drift ratio of structures under FF-7 and FF-12 earthquake ground motion (MCE level)

4) The utilization of Fe-SMA energy dissipation devices would slightly amplify the PFA response. However, when they are installed in frames with high-strength steels, the PFA responses are reduced significantly, even lower than those of conventional yielding structural systems, suggesting that HSSF is an ideal frame type used in combination with Fe-SMA energy dissipation devices.

Apart from the above conclusions, additional discussions on possible future works are made herein. For example, it has been noticed that the strength degradation behavior of the Fe-SMA U-shaped strips is different from that of its mild steel counterparts, a case which may result from the difference between their fatigue-induced failure mechanisms. Efforts are being devoted to finding the reason behind the phenomenon, and a series of micro-mechanical level experiments have been conducted by the authors, where the results will be reported in future papers. In addition, the seismic community has been aware of the failure risk of excessive inelastic deformation caused by long duration earthquakes, and Fe-SMA-based energy dissipation devices are seen as a potential strategy to solve the fatigue problem. Further works are required in investigating both the fatigue demand and supply of the proposed new systems.

Acknowledgements
The financial supports from the National Natural Science Foundation of China (NSFC) with Grant Nos. 52078359 and 51820105013 are gratefully acknowledged. Support for this study was also provided by the Shanghai Rising-Star Program (20QA1409400) and the Fundamental Research Funds for the Central Universities.

Authors' contributions
Zhe-Xi Zhang: Methodology, Investigation, Software, Data curation, Formal analysis, Visualization, Writing – original draft. Cheng Fang: Conceptualization, Project administration, Supervision, Resources, Writing – review & editing, Funding acquisition. Jie Zhang: Supervision, Resources, Methodology, Investigation. Yuelin Zhang: Supervision, Methodology, Investigation. Yuanmu Li: Supervision, Methodology. All authors have read and agreed to the published version of the manuscript.

Funding
The financial supports from the National Natural Science Foundation of China (NSFC) with Grant Nos. 52078359 and 51820105013 are gratefully acknowledged. Support for this study was also provided by the Shanghai Rising-Star Program (20QA1409400) and the Fundamental Research Funds for the Central Universities.

Availability of data and materials
The datasets are available from the corresponding author on reasonable request.

Declarations

Ethics approval and consent to participate
Not applicable.

Consent for publication
Not applicable.

Competing interests
The authors declare that they have no competing interests.

Received: 17 November 2022 Revised: 25 December 2022 Accepted: 28 December 2022
Published online: 24 January 2023

References

1. Razafindrakoto HNT, Bradley BA, Graves RW (2018) Broadband Ground-Motion Simulation of the 2011 M-w 6.2 Christchurch, New Zealand, Earthquake. B Seismol Soc Am 108(4):2130–2147
2. Lab K (1995) Field survey report on structural damage during the 1995 Hyogoken-Nanbu earthquake. Kuwamura Lab, School of Engineering. The University of Tokyo, Tokyo
3. McCormick J, Aburano H, Ikenaga M, Nakashima M (2008) Permissible residual deformation levels for building structures considering both safety and human elements. 14th World Conference on Earthquake Engineering. Seismological Press of China, Beijing
4. Benmokrane B, Xu HX, Nishizaki I (1997) Aramid and carbon fibre-reinforced plastic prestressed ground anchors and their field applications. Can J Civ Eng 24(6):968–985
5. Ricles JM, Sause R, Garlock MM, Zhao C (2001) Posttensioned seismic-resistant connections for steel frames. J Struct Eng-Asce 127(2):113–121
6. Ricles JM, Sause R, Peng SW, Lu LW (2002) Experimental evaluation of earthquake resistant posttensioned steel connections. J Struct Eng 128(7):850–859
7. Kam WY, Pampanin S, Palermo A, Carr A (2006) Advanced flag-shaped systems for high seismic performance. 1st European Conference on Earthquake Engineering, Geneva
8. Garlock MM, Sause R, Ricles JM (2007) Behavior and design of posttensioned steel frame systems. J Struct Eng 133(3):389–399
9. Ma HW, Wilkinson T, Cho CD (2007) Feasibility study on a self-centering beam-to-column connection by using the superelastic behavior of SMAs. Smart Mater Struct 16(5):1555–1563
10. Christopoulos C, Tremblay R, Kim H-J, Lacerte M (2008) Self-centering energy dissipative bracing system for the seismic resistance of structures: development and validation. J Struct Eng 134(1):96–107
11. Tsai KC, Chou CC, Lin CL, Chen PC, Jhang SJ (2008) Seismic self-centering steel beam-to-column moment connections using bolted friction devices. Earthquake Eng Struct Dynam 37(4):627–645
12. Chou CC, Chung PT (2014) Development of cross-anchored dual-core self-centering braces for seismic resistance. J Constr Steel Res 101:19–32
13. Fang C, Liang D, Zheng Y, Lu SY (2022) Seismic performance of bridges with novel SMA cable-restrained high damping rubber bearings against near-fault ground motions. Earthquake Eng Struct Dynam 51(1):44–65
14. Fang C, Zheng Y, Chen J, Yam MCH, Wang W (2019) Superelastic NiTi SMA cables: Thermal-mechanical behavior, hysteretic modelling and seismic application. Eng Struct 183:533–549
15. Fang C, Liang D, Zheng Y, Yam MCH, Sun R (2020) Rocking bridge piers equipped with shape memory alloy (SMA) washer springs. Eng Struct 214:110651
16. Zheng Y, Fang C, Liang D, Sun R (2020) An innovative seismic-resilient bridge with shape memory alloy-washer-based footing rocking RC piers. J Intell Mater Syst Struct 32(5):549–567
17. Wang W, Fang C, Zhang A, Liu X (2019) Manufacturing and performance of a novel self-centring damper with shape memory alloy ring springs for seismic resilience. Struct Control Health Monit 26(5):e2337
18. Wang W, Fang C, Zhao Y, Sause R, Hu S, Ricles J (2019) Self-centering friction spring dampers for seismic resilience. Earthquake Eng Struct Dynam 48(9):1045–1065
19. Fang C, Yam MCH, Chan T-M, Wang W, Yang X, Lin X (2018) A study of hybrid self-centring connections equipped with shape memory alloy washers and bolts. Eng Struct 164:155–168
20. Qiu CX, Zhu SY (2017) Shake table test and numerical study of self-centering steel frame with SMA braces. Earthquake Eng Struct Dynam 46(1):117–137
21. Chen J, Wang W, Fang C (2022) Manufacturing, testing and simulation of novel SMA-based variable friction dampers with enhanced deformability. J Build Eng 45:103513
22. Ping Y, Fang C, Shi F, Wu H, Yam MCH, Chen Y (2022) Experimental and numerical studies on SMAviscoelastic hybrid self-centering braces. Smart Mater Struct 31:095048 (20pp)
23. Zhang Z-X, Ping Y, He X (2022) Self-Centering Shape Memory Alloy-Viscoelastic Hybrid Braces for Seismic Resilience. Materials 15(2349):15072349
24. Ping Y, Fang C, Chen Y, Yam MCH (2021) Seismic robustness of self-centering braced frames suffering tendon failure. Earthquake Eng Struct Dynam 50(6):1671–1691
25. Zhang Z-X, Zhang J, Wu H, Ji Y, Kumar DD (2022) Iron-Based Shape Memory Alloys in Construction: Research, Applications and Opportunities. Materials 15(5):1723
26. Fang C, Ping Y, Zheng Y, Chen Y (2021) Probabilistic economic seismic loss estimation of steel braced frames incorporating emerging self-centering technologies. Eng Struct 241:112486
27. Fang C, Ping Y, Chen Y, Yam MCH, Chen J, Wang W (2020) Seismic Performance of Self-centering Steel Frames with SMA-viscoelastic Hybrid Braces. Journal of Earthquake Engineering 26(10):1–28
28. Rosa DIH, Hartloper A, de Castro e Sousa A, Lignos DG, Motavalli M, Ghafoori E (2021) Experimental behavior of iron-based shape memory alloys under cyclic loading histories. Constr Build Mater 272:121712
29. Sawaguchi T, Maruyama T, Otsuka H, Kushibe A, Inoue Y, Tsuzaki K (2016) Design Concept and Applications of Fe–Mn–Si-Based Alloys—from Shape-Memory to Seismic Response Control. Mater Trans 57(3):283–293
30. Wang W, Fang C, Ji Y, Lu Y (2022) Experimental and numerical studies on novel Fe-Mn-Si alloy dampers for enhanced low-cycle fatigue resistance. J Struct Eng 148:04022170
31. Inoue Y, Kushibe A, Umemura K, Mizushima Y, Sawaguchi T, Nakamura T, Otsuka H, Chiba Y (2020) Fatigue-resistant Fe-Mn-Si-based alloy seismic dampers to counteract long-period ground motion. Japan Architectural Review 4(1):76–87
32. Ghowsi AF, Sahoo DR, Kumar PCA (2020) Cyclic tests on hybrid buckling-restrained braces with Fe-based SMA core elements. J Constr Steel Res 175:106323
33. Fang C, Wang W, Ji Y, Yam MCH (2021) Superior low-cycle fatigue performance of iron-based SMA for seismic damping application. J Constr Steel Res 184:106817
34. Zhang J, Fang C, Yam MC, Lin C (2022) Fe-Mn-Si alloy U-shaped dampers with extraordinary low-cycle fatigue resistance. Eng Struct 264:114475
35. Wang B, Zhu S (2021) Cyclic behavior of iron-based shape memory alloy bars for high-performance seismic devices. Eng Struct 252:113588
36. Wang B, Zhu S (2018) Cyclic tension–compression behavior of superelastic shape memory alloy bars with buckling-restrained devices. Constr Build Mater 186:103–113
37. Shi G, Zhao H, Gao Y (2022) Development of triple grades hybrid high-performance steel structure (TGHSS): Concept and experiments. Eng Struct 266:114654
38. OpenSees (2012) Open system for earthquake engineering simulation. http://opensees.berkeley.edu/.

39. Taiyari F, Mazzolani F, Bagheri S (2019) A proposal for energy dissipative braces with U-shaped steel strips. J Constr Steel Res 154:110–122
40. Kato S, Kim Y-B (2006) A finite element parametric study on the mechanical properties of J-shaped steel hysteresis devices. J Constr Steel Res 62:802–811
41. Bandstra JP (1983) Comparison of equivalent viscous damping and nonlinear damping in discrete and continuous vibrating systems. J Vib Acoust Stress Reliability Design Transactions Asme 105:382–392
42. ABAQUS (2013) Abaqus analysis user's guide, version 6.13. Dassault Systèmes Simulia Corp, Providence
43. Chaboche JL (2008) A review of some plasticity and viscoplasticity constitutive theories. Int J Plast 24(10):1642–1693
44. McKenna F (2011) OpenSees: A Framework for Earthquake Engineering Simulation. Comput Sci Eng 13(4):58–66
45. American Society of Civil Engineers (ASCE) (2016) Minimum Design Loads for Buildings and Other Structures. Reston
46. Federal Emergency Management Agency (2012) Seismic Performance Assessment of Buildings FEMA P-58-1. Methodology. Washington
47. Xiang Y, Zhang YJ, Xu F, Li GQ (2022) Feasibility of a nonlinear spectral approach for peak floor acceleration of multi-story bilinear hysteretic buildings. Bull Earthquake Eng 21:349–373

Publisher's Note